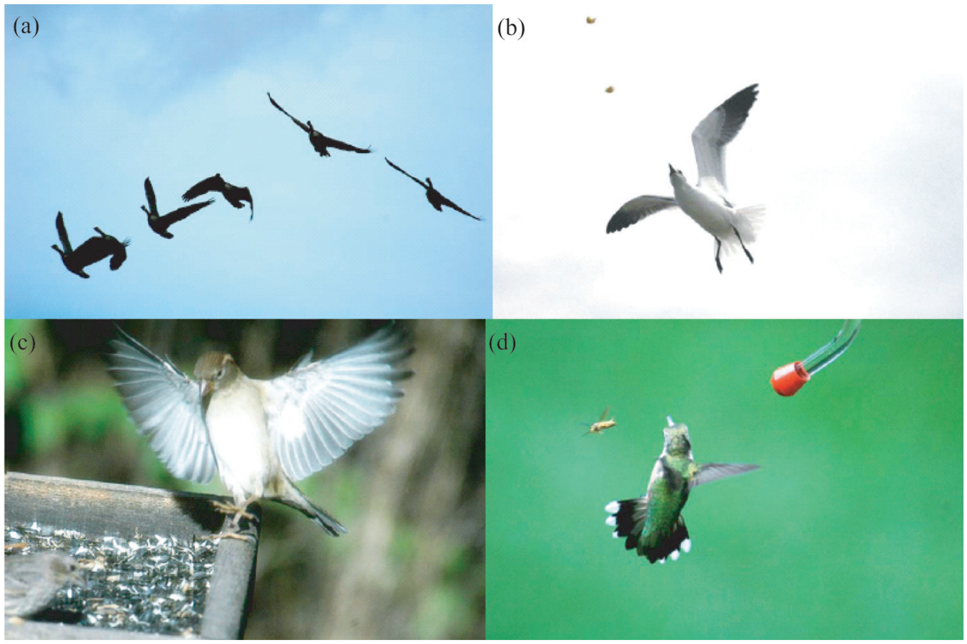

Plate I. Maneuvering capabilities of natural flyers. (a) Canada geese's response to wind gust; (b) speed control and target tracking of a seagull; (c) precision touch-down of a finch; (d) a hummingbird defending itself against a bee.

Plate II. Natural flyers can track target precisely and instantaneously. Shown here are hummingbirds using flapping wings, contoured body, and tail adjustment to conduct flight control.

Plate III. Natural flyers synchorize wings, body, legs, and tail to take off, on water (top), from land (middle), and off tree (bottom).

Plate IV. Birds such as seagulls glide while flexing their wings to adjust their speed as well as to control their direction.

Plate V. On landing, birds fold their wings to reduce lift, and flap to accommodate wind gusts and to adjust for their available landing areas.

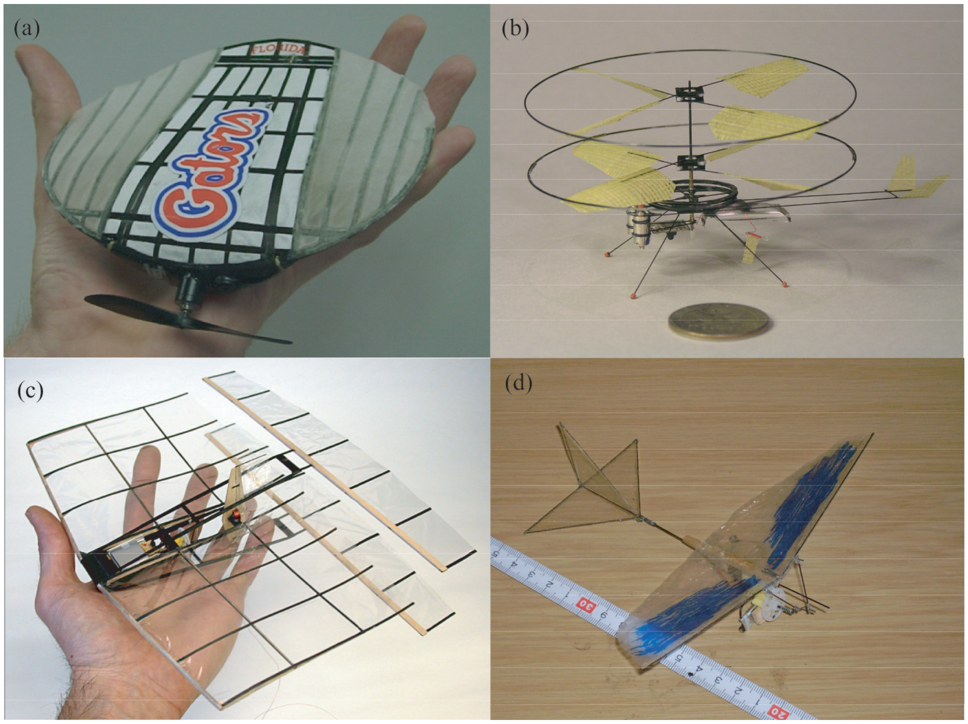

Plate VI. Representative MAVs. (a) flexible fixed wing (Ifju et al., 2002); (b) rotary wing (http://www.proxflyer.com); (c) hybrid flapping-fixed wing, using fixed wing for lift and flapping wing for thrust (Jones and Platzer, 2006); and (d) flapping wing for both lift and thrust (Kawamura et al., 2006).

Plate VII. Illustration of biological flapping-wing patterns: forward and back strokes, and flexible- and asymmetric-wing motions.

Plate VIII. Dragonfly wings exbit both flexibility and anisotropic, corrugated structuures. In the lower picture, shown on the left is the hind wing and the right is the fore wing.

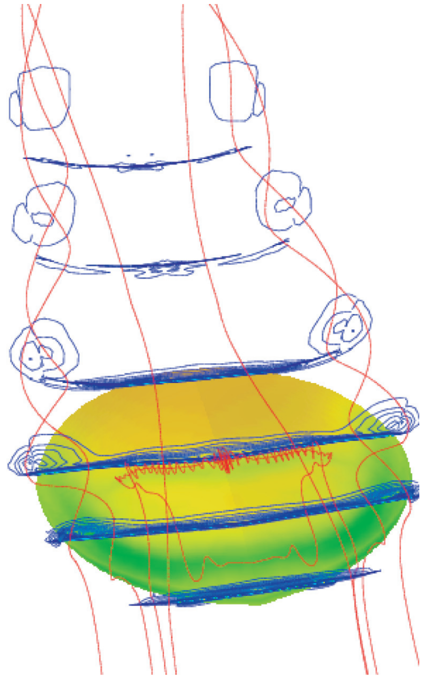

Plate IX. Streamlines and vortices for rigid wing at $\alpha = 39°$. The vortical structures are shown on selected planes (Lian et al., 2003b).

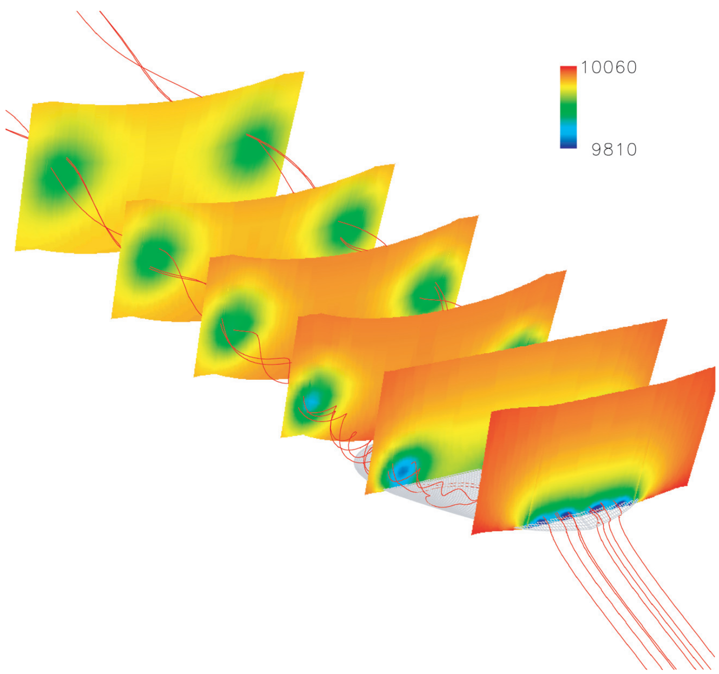

Plate X. Pressure distribution around the rigid wing in the cross sections with streamlines at angle of attack of 39° (Lian et al., 2003b).

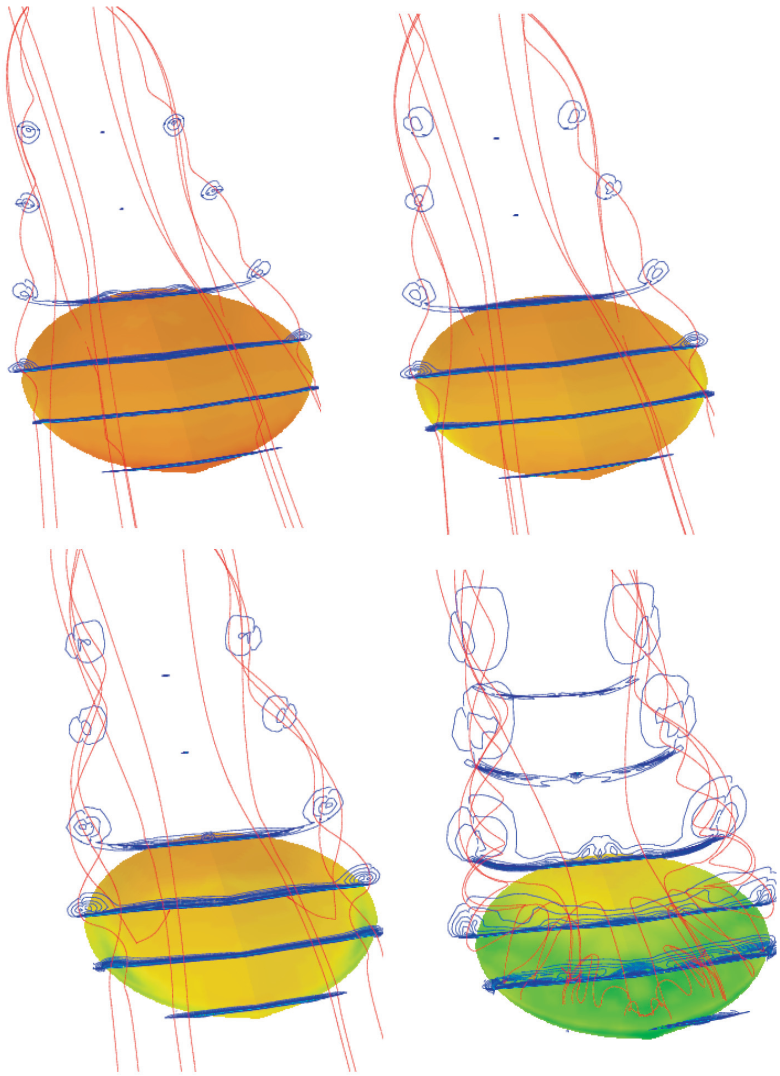

Plate XI. Evolution of flow pattern for rigid wing versus angles of attack. (From left to right, top to bottom, 6°, 15°, 27°, and 51°) (Lian and Shyy, 2005).

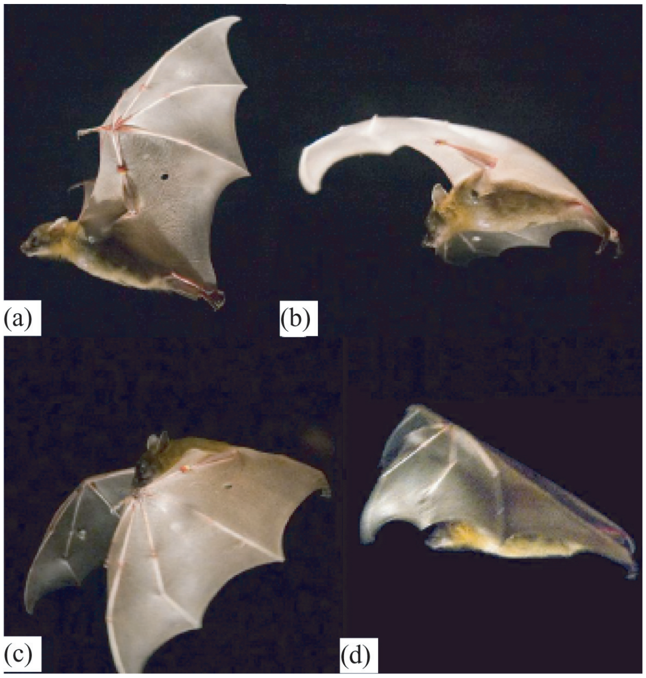

Plate XII. A bat *(Cynopterus brachyotis)* in flight. (a) beginning of downstroke, head forward, tail backward, the whole body is stretched and lined up in a straight line; (b) middle of downstroke, the wing is highly cambered; (c) end of downstorke (also beginning of upstroke), the wing is still cambered. A large part of the wing is in front of the head and the wing is going to be withdrawn to its body; (d) Middle of upstroke, the wing is folded towards the body, from Tian et al. (2006).

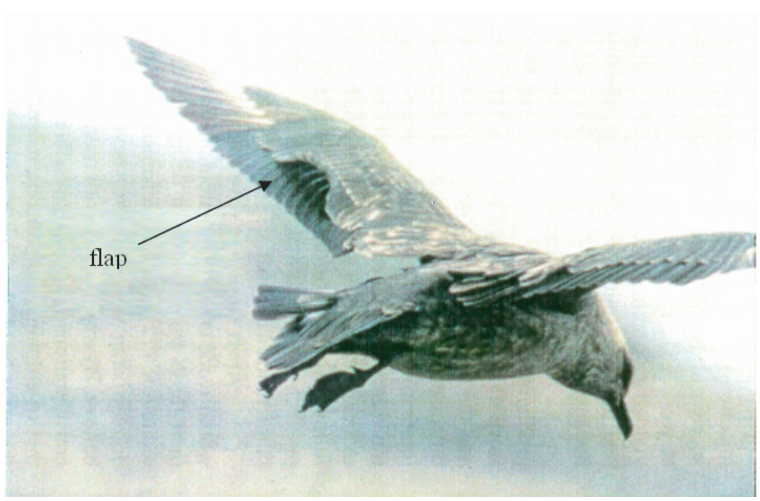

Plate XIII. The flexible covert feathers acting like self-activated flaps on the upper wing surface of a skua. Photo from Bechert et al. (1997).

Plate XIV. Vortices structure behind a stationary NACA 0012 (Lai and Platzer, 1999).

(a) h = 0.0125 (kh = 0.098)

(b) h = 0.025 (kh = 0.196)

(c) h = 0.05 (kh = 0.393)

Plate XV. Vortex patterns for a NACA 0012 airfoil oscillated in plunge for a freestream velocity of about 0.2 m/s, a frequency of $f = 2.5$ Hz ($k = 7.85$), and various amplitudes of oscillation (Lai and Platzer, 1999).

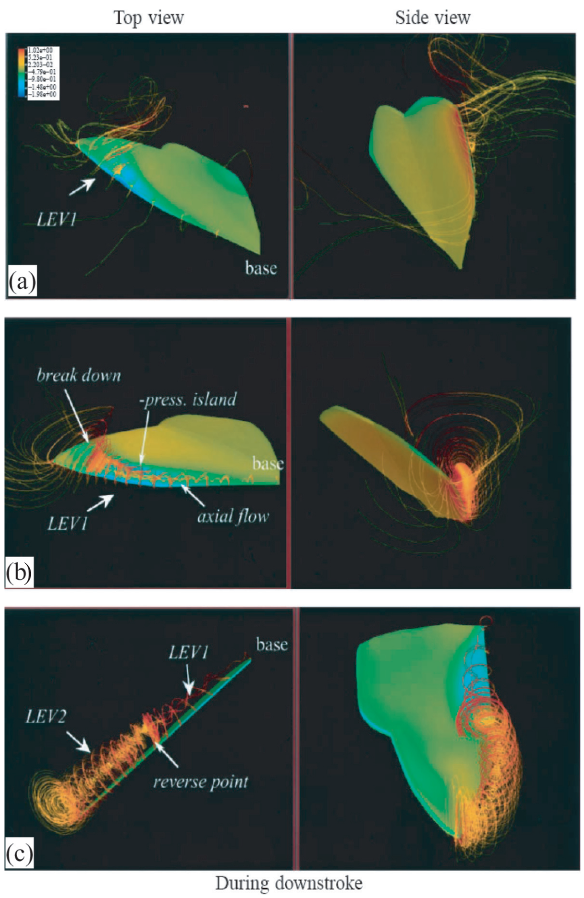

Plate XVI. Wing surface pressure and streamlines revealing the vortical structures for the 3D numerical simulation of a hovering hawkmoth (Liu et al., 1998). (a) Positional angle ϕ=30°; (b) ϕ=0°; (c) ϕ=-36°. Reynolds number is approx. 4000 and the reduced frequency k is 0.37. Here LEV is the leading edge vortex.

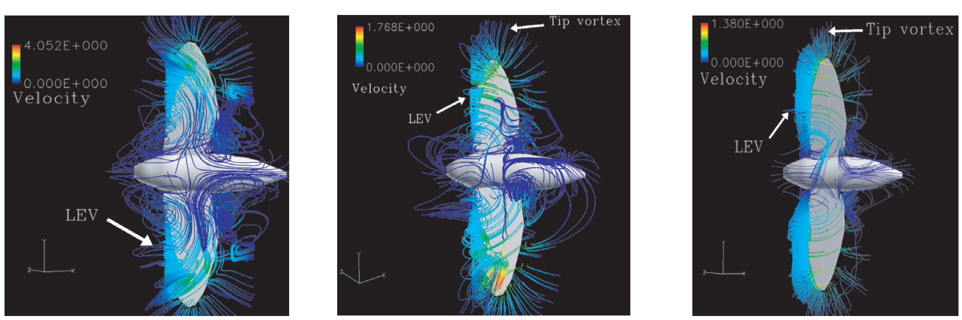

(a) Re_{f3}=6000 (b) Re_{f3}=120 (c) Re_{f3}=10

Plate XVII. Numerical results of leading edge vortical structures at different Reynolds numbers.

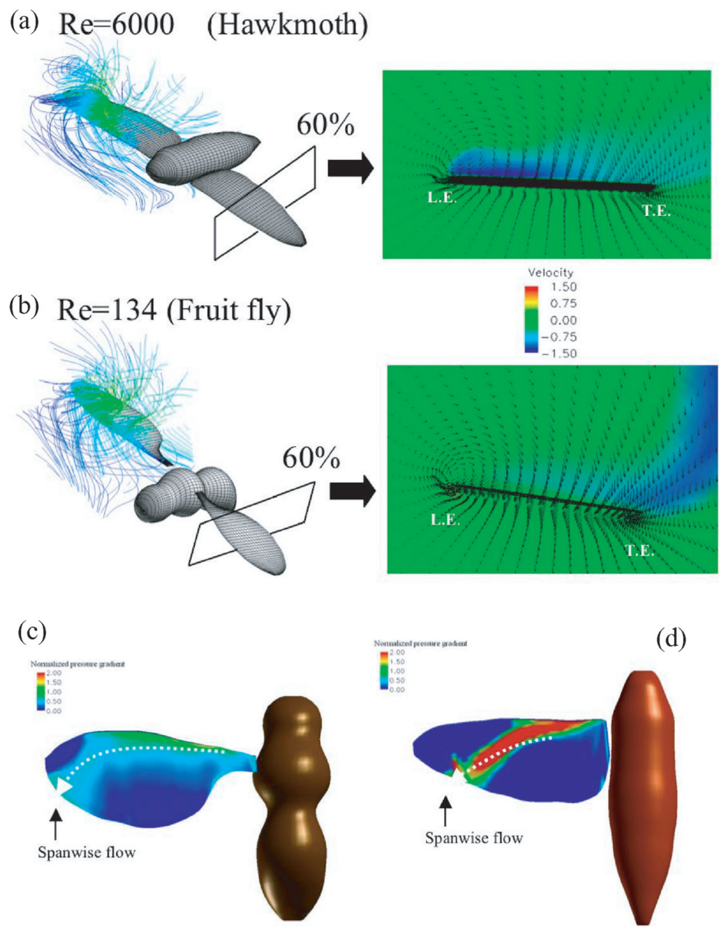

Plate XVIII. Comparison of near-field flow fields between a fruit fly and a hawkmoth. Wing-body computational model of (a) a hawkmoth ($Re_{f3} = 6000$, $U_{ref} = 5.05$ m/s, $c_m = 1.83$ cm), and (b) a fruit fly model ($Re_{f3} = 134$, $U_{ref} = 2.54$ m/s, $c_m = 0.78$ mm), with the LEVs visualized by instantaneous streamlines and the corresponding velocity vectors in a plane cutting through the left wing at 60% of the wing length; pressure gradient contours on the wing surface for (c) a fruit fly, and (d) a hawkmoth. The pressure gradient indicates the direction of the spanwise flow.

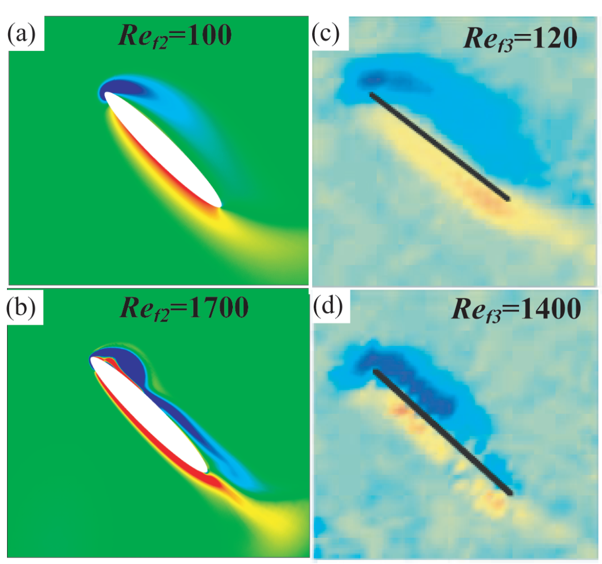

Plate XIX. Vortical flow structures for pitch-up airfoils: (a) and (b) computational results for flow over a 2D elliptic airfoil undergoing "water treading" hovering at two Reynolds numbers. The airfoil position corresponds to the mid-stroke, where the pitch angle reaches the maximum value; (c) and (d) experimental vorticity field side views for a fruit fly modeled wing at 0.65R at mid-stroke. The experimental information in (c) and (d) is reprinted from Birch et al. (2004).

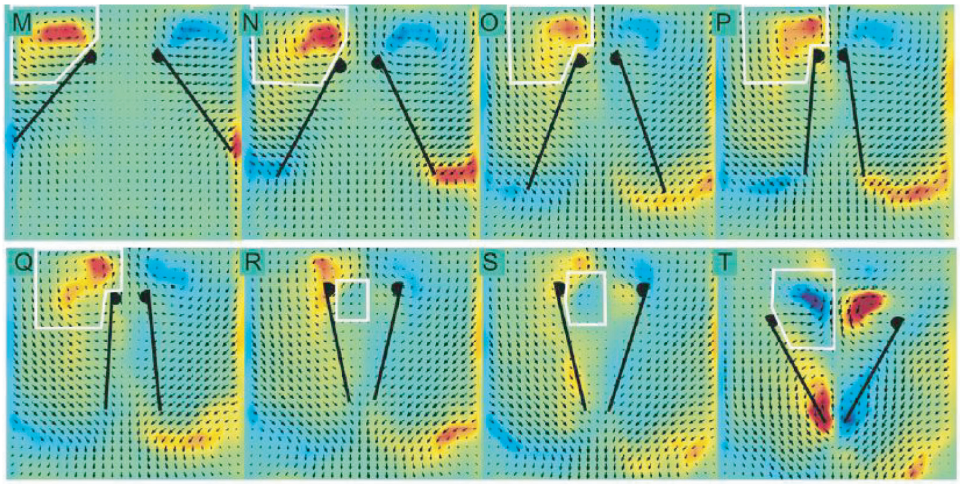

Plate XX. Experiment of clap-and-fling by two wings (M–T) using clap-and-fling wing beat pattern in the robotic wing. Vorticity is plotted according to the pseudo color code and arrows indicate the magnitude of fluid velocity; longer arrows signifying larger velocities, from Lehmann et al. (2005) with permission.

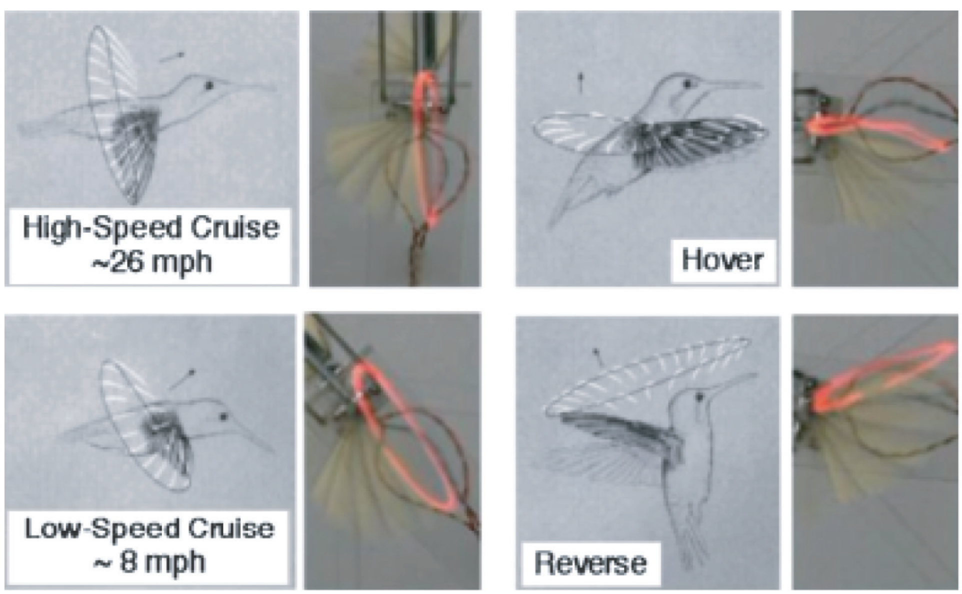

Plate XXI. Comparison of the wingtip trajectories produced by the vibratory flapping system with those exhibited by hummingbirds in various flight modes, from Raney and Slominski (2004).

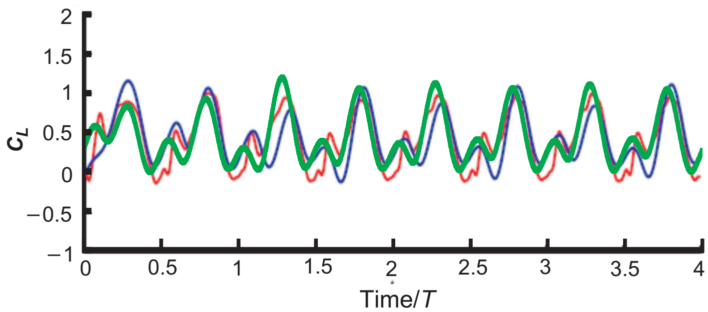

Plate XXII. Numerical and experimental results of the flapping motion of a fruit fly: red, experimental results of Dickinson and Birch (Wang et al., 2004); Blue, numerical solution of Wang et al. (2004); green, numerical solution of Tang et al. (2007). $h_a/c = 1.4$, $\alpha_a = 45^\circ$, $Re_{f2} = 75$, $k = 0.357$.

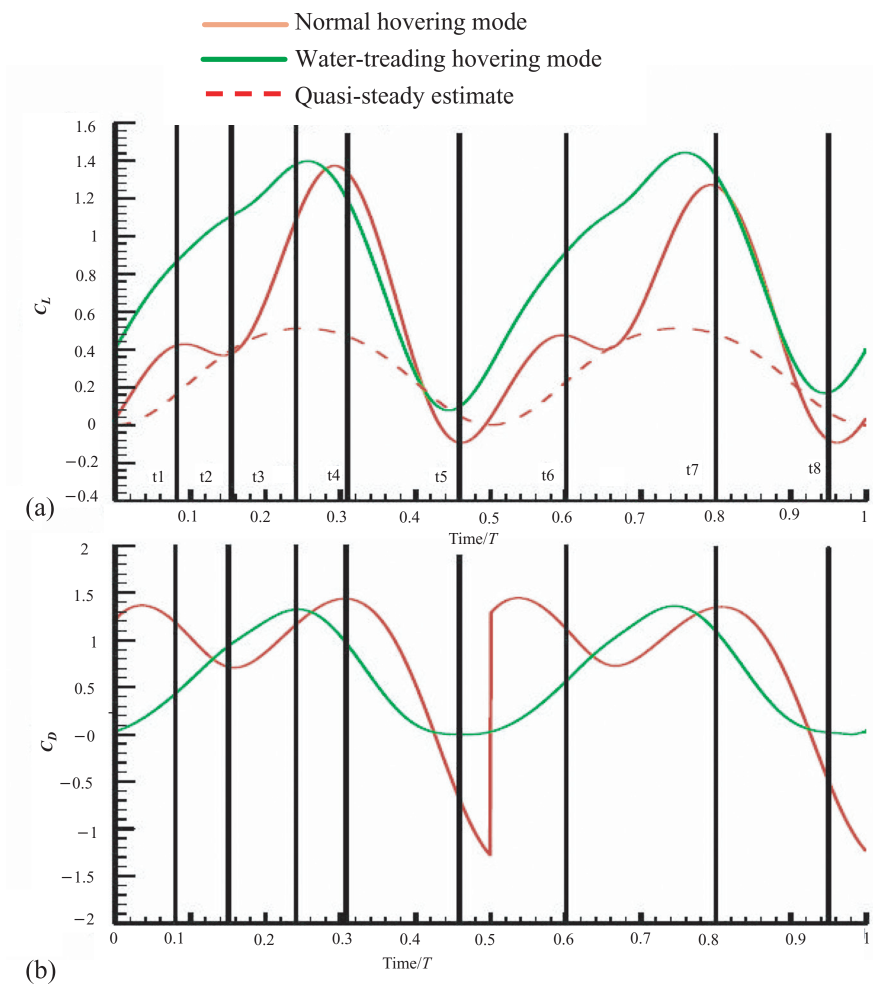

Plate XXIII. One cycle force history for two hovering modes and quasi-steady value of normal hovering mode. $h_a/c = 1.4$, $\alpha_a = 45^\circ$, $k = 0.357$, and $Re_{f2} = 100$. (a) Lift coefficient, (b) drag coefficient. The selected normalized time instants are t1 = 0.08, t2 = 0.17, t3 = 0.25, t4 = 0.31, t5 = 0.45, t6 = 0.60, t7 = 0.80, t8 = 0.94.

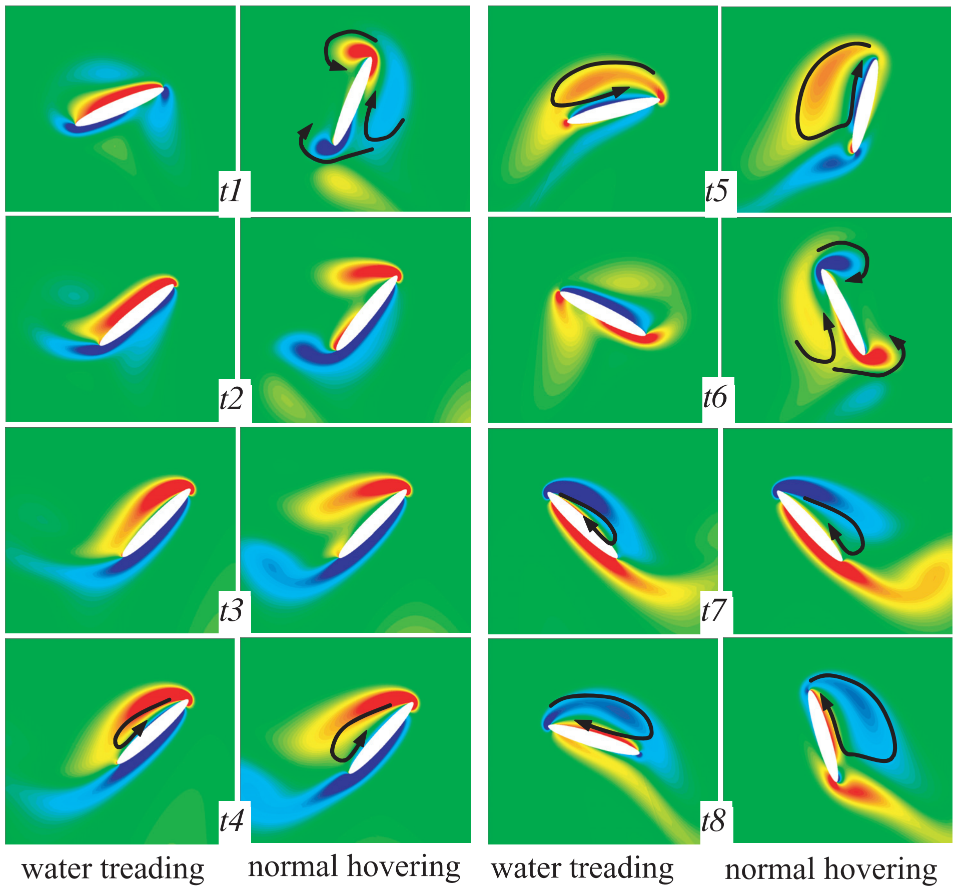

Plate XXIV. Vorticity contours for two hovering modes. $h_a/c = 1.4$, $\alpha_a = 45°$, $k = 0.357$ and $Re_{f2} = 100$. Red: counter-clockwise vortices, Blue: clockwise vortices. The flow snapshots (t1 to t8) correspond to the time instants defined in Figure 4-38. Adopted from Tang et al. (2007).

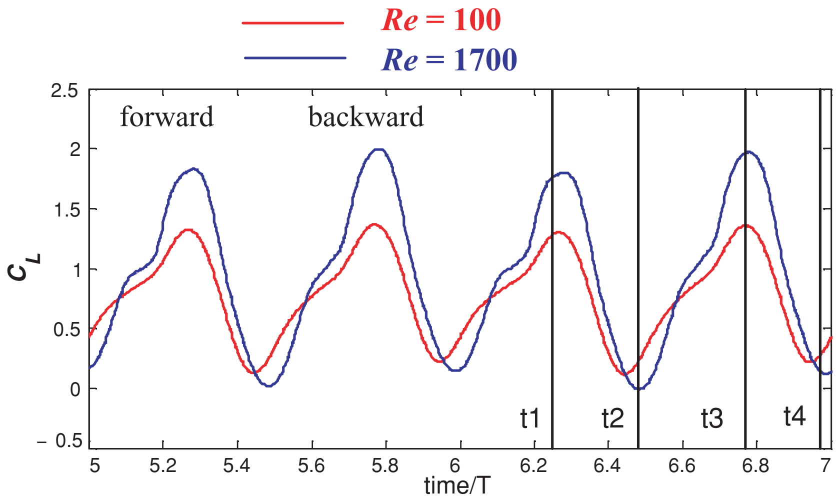

Plate XXV. Lift coefficient for the water-treading mode. $h_a/c = 1.4$, $\alpha_a = 45°$, $k = 0.357$, and Reynolds numbers of 100 and 1700. The selected normalized time instants are t1 = 6.25, t2 = 6.48, t3 = 6.77, t4 = 6.97.

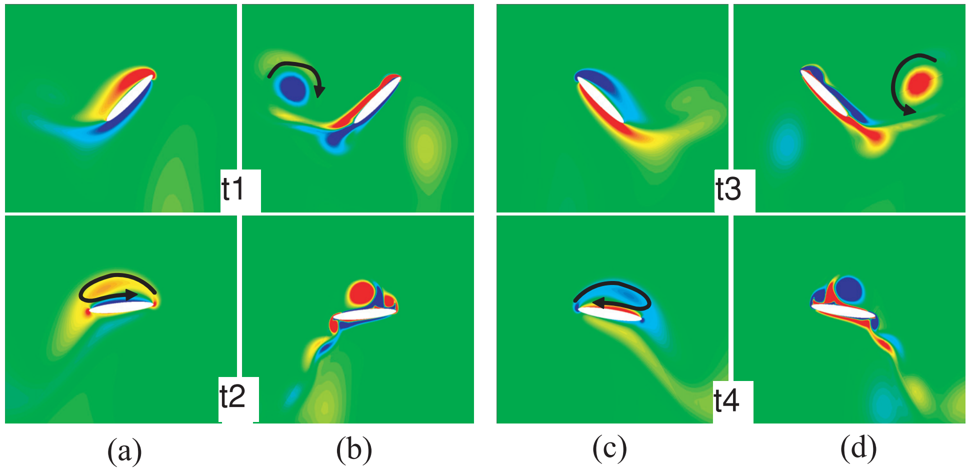

Plate XXVI. Vorticity contours for the "water treading" mode. $h_a/c = 1.4$, $\alpha_a = 45°$, $k = 0.357$. Red = counter-clockwise vortices, Blue = clockwise vortices. (a), (c) Reynolds number = 100; (b), (d) Reynolds number = 1,700. The flow snapshots (t1 to t4) correspond to the time instants defined in Figure 4.40.

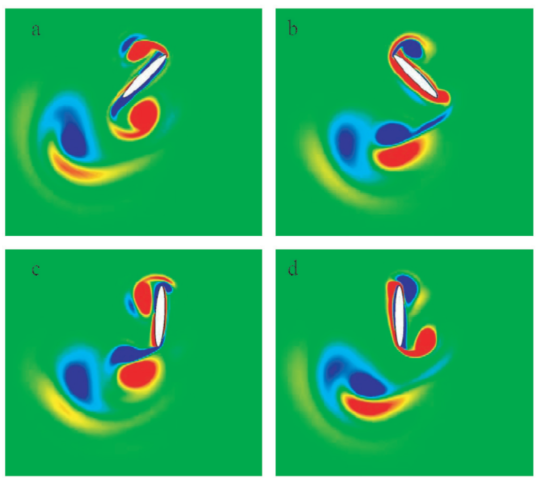

Plate XXVII. Vorticity contours at two corresponding positions during forward (a) and (c) and backward (b) and (d) stroke. Stroke amplitude $h_a/c = 0.25$, pitch angle amplitude $\alpha_a = 45°$ and $Re_{f2} = 300$.

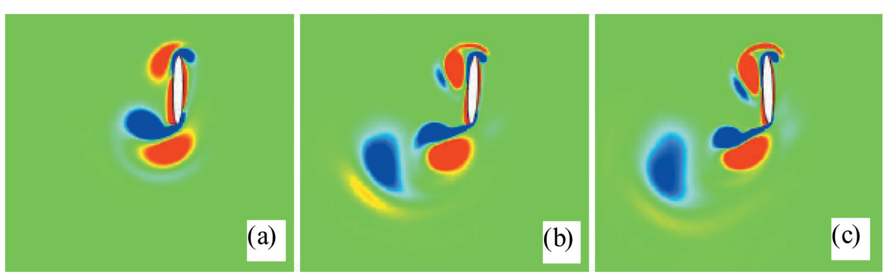

Plate XXVIII. Vorticity contours at time $/T = 5.5$ and three different Reynolds number with a stroke amplitude $h_a/c = 0.25$ and $\alpha_a = 45°$: (a) $Re_{f2} = 75$; (b) $Re_{f2} = 300$; (c) $Re_{f2} = 500$.

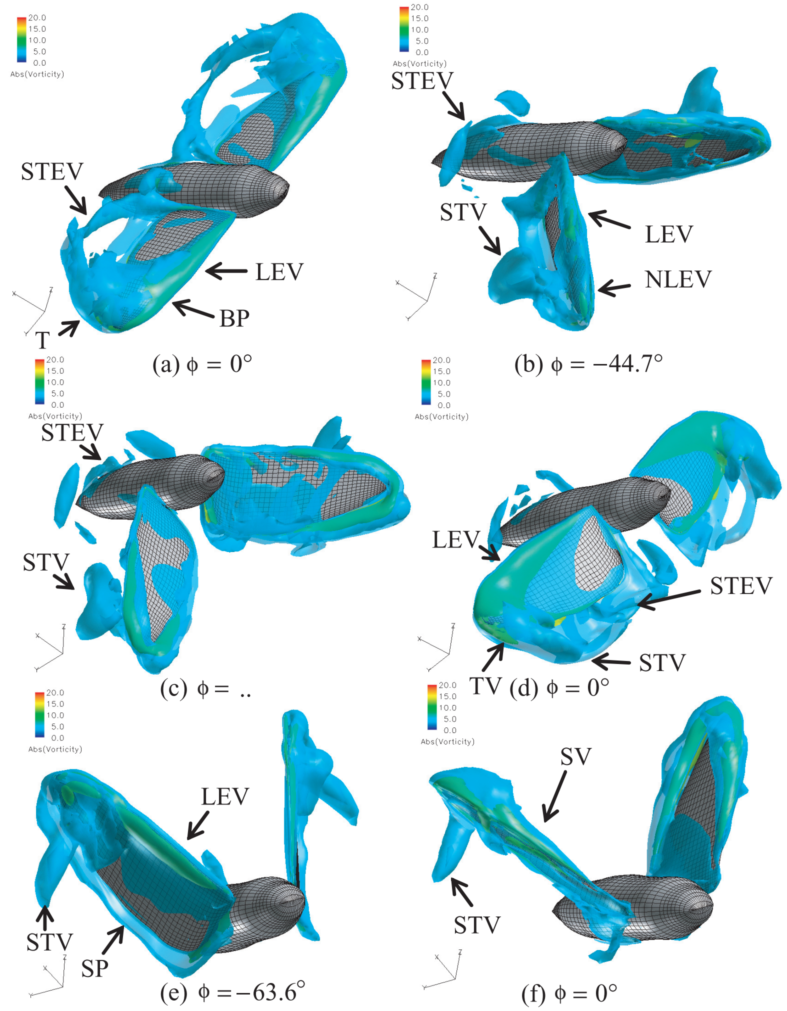

Plate XXIX. Iso-vorticity surfaces (absolute vorticity strengths: 4=green, 13=blue) around flapping wings and body of a hawkmoth during a flapping cycle. Shedding TV (STV) shedding TEV (STEV), new LEV (NLEV), stopping-vortex (SPV), starting-vortex (SV), and breakdown point.